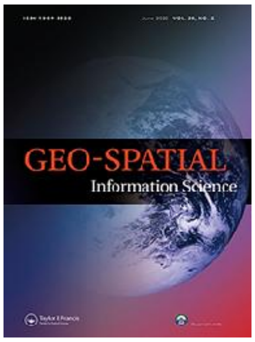

Geo-spatial Information Science

ISSN: (Print) (Online) Journal homepage: https://www.tandfonline.com/loi/tgsi20

The ATL08 as a height reference for the global digital elevation models

Nahed Osama, Zhenfeng Shao, Yue Ma, Jianguo Yan, Yewen Fan, Shaimaa Magdy Habib & Mohamed Freeshah

GEO-SPATIAL INFORMATION SCIENCE
https://doi.org/10.1080/10095020.2022.2087108

The ATL08 as a height reference for the global digital elevation models

Nahed Osama[a,b], Zhenfeng Shao[a], Yue Ma[c], Jianguo Yan[a], Yewen Fan[a], Shaimaa Magdy Habib[b] and Mohamed Freeshah[d,e]

[a]State Key Laboratory of Information Engineering in Surveying, Mapping and Remote Sensing, Wuhan University, Wuhan, China; [b]Department of Aviation and Aerial Photography, National Authority for Remote Sensing and Space Sciences, Cairo, Egypt; [c]School of Electronic Information, Wuhan University, Wuhan, China; [d]Department of Surveying Engineering, Faculty of Engineering at Shoubra, Benha University, Cairo, Egypt; [e]School of Geodesy and Geomatics, Wuhan University, Wuhan, China

ABSTRACT
High-quality height reference data are embedded in the accuracy verification processes of most remote sensing terrain applications. The Ice, Cloud, and Land elevation Satellite 2 (ICESat-2)/ATL08 terrain product has shown promising results for estimating ground heights, but it has not been fully evaluated. Hence, this study aims to assess and enhance the accuracy of the ATL08 terrain product as a height reference for the newest versions of the Advanced Spaceborne Thermal Emission and Reflection Radiometer (ASTER), the Shuttle Radar Topography Mission (SRTM), and TanDEM-X (TDX) DEMs over vegetated mountainous areas. We used uncertainty-based filtering method for the ATL08 strong and weak beams to enhance their accuracy. Then, the results were evaluated against a reference airborne LiDAR digital terrain model (DTM), by selecting 10,000 points over the entire area and comparing the accuracy of ASTER, SRTM, and TDX DEMs assessed by the LiDAR DTM to the accuracy of the ASTER, SRTM, and TDX DEMs assessed by the ATL08 strong beams, weak beams, and all beams. We also detected the impact of the terrain aspect, slope, and land cover types on the accuracy of the ATL08 terrain elevations and their relationship with height errors and uncertainty. Our findings show the accuracy of the ATL08 strong beams was enhanced by 43.91%; while the weak beams accuracy was enhanced by 74.05%. Furthermore, slope strongly influenced ATL08 height errors and height uncertainty; especially on the weak beams. The errors induced by the slope significantly decreased when the uncertainty levels were reduced to <20 m. The evaluations of ASTER, SRTM, and TDX DEMs by ATL08 strong and weak beams are close to those assessed by LiDAR DTM points within 0.6 m for the strong beams. These findings indicate that ATL08 strong beams can be used as a height reference over vegetated mountainous regions.

ARTICLE HISTORY
Received 13 December 2021
Accepted 2 June 2022

KEYWORDS
ATL08; digital elevation model (DEM); digital terrain model (DTM); slope; land cover; terrain; validation; ICESat-2

1. Introduction

Geomorphology, mass movement, 3D visualizations, surface analysis, and other related sciences depend on remote sensing for terrain elevation data. Acquiring accurate reference data at large-scale is quite challenging because ground-based field surveys are often impractical or too expensive, especially for large extensive regions (Henrys and Jarvis 2019). High-resolution space-based remote sensing has an advantage over other techniques, as it provides wider spatial coverage at minimum cost. Researchers have investigated the accuracy of different versions of global digital elevation models (DEMs) in comparative studies. DEMs were evaluated against Global Navigation Satellite Systems (GNSS) elevation data (Athmania and Achour 2014; Brunt, Neumann, and Larsen 2019) and to high-quality altimetry measurements (Boulton and Stokes 2018; Zhang et al. 2019). Every several years, new versions of these DEMs are released with enhancements related to data voids, spatial resolution, interpolation algorithms, and accuracy. These new versions require an ongoing global source for continuous validation and assessment.

Since 2003, the Geoscience Laser Altimeter System (GLAS), i.e. a full waveform LiDAR, borne on the Ice, Cloud, and Land Elevations Satellite (ICESat) has provided high-accuracy global elevations to measure the ice sheets mass, topographic heights as well as vegetation attributes (Salas 2021; Brenner, DiMarzio, and Zwally 2007). The accuracy of the ICESat data has been evaluated using ground truth data; its vertical accuracy ranged between 0.12 m and 0.50 m depending on the vegetation cover (Fricker et al. 2005; Braun and Fotopoulos 2007; Siegfried, Hawley, and Burkhart 2011). Thus, ICESat data were used as ground control data in evaluations of global DEMs such as ASTER GDEM V2 and TDX DEMs (Hueso González et al. 2010; Satgé et al. 2015). In the later part of 2018, ICESat-2 was launched to continue the work of the earlier mission with the aim of providing a higher accuracy, precision, and wider spatial coverage for height retrieval. The Advanced Topographic Laser

CONTACT Zhenfeng Shao shaozhenfeng@whu.edu.cn

Altimeter System (ATLAS) is a photon-counting LiDAR system borne on the ICESat-2. The ATLAS laser beam is divided into six dissimilar energy beams, three of them are four times higher in energy than the others (Hsu et al. 2021; Neuenschwander and Magruder 2016). The photon data released by ATLAS are exposed to many factors that decrease its energy and introduce ranging errors, such as atmospheric scattering and attenuation, solar background effect, degree of the surface reflectance, and laser interaction with different land covers. Consequently, the rate of the received signal backscatters is low and the noise rate is high, particularly during the daytime with the higher solar background (Neumann et al. 2019). All these errors greatly affect the accuracy of the different products derived from ATLAS raw data.

The ICESat-2/ATL08 product contains 3-A level elevation data derived from the ATL03 raw data, and provides two height categories representing the terrain and the relative canopy heights. The research community has investigated the accuracy and potential applications of the ATL08 product, finding that it provides a promising means to retrieve the terrain and canopy heights (Lin et al. 2020; Neuenschwander et al. 2019; Osama et al. 2021), estimate terrain slope (Zhu et al. 2020), filtering the existing global DEMs with the aid of LandSat images (Magruder, Neuenschwander, and Klotz 2021), map forest fires (Liu, Popescu, and Malambo 2020), and replace Lidar data in global DEMs assessment (Guth and Geoffroy 2021). Vernimmen et al created the Global LiDAR Lowland DTM (GLL_DTM_v1) from the ATL08 terrain product for flood risk assessment. This DTM simulates the gridded elevations for the terrain and canopy heights that will be included in the future ICESat-2/ATL018 product. The vertical accuracy of the GLL_DTM_v1 was up to 0.53 m for 83.4% of the study area, which is higher than the other available global DEMs accuracies in the test region (Vernimmen, Hooijer, and Pronk 2020). However, GLL_DTM_v1 DTM has a course resolution of (5 km × 5 km) and it failed to take full advantage of the 100 m segment of the ATL08- terrain product. In addition, this research (Vernimmen, Hooijer, and Pronk 2020) did not take into account that adding the ATL08 weak beams to the strong beams may reduce the accuracy of the produced model. Especially, since the resampling process at 5 km may keep the weak beams data and remove some of the strong beams' data.

The absolute vertical accuracy of ATL08-terrain product ranges from the sub-meter level to several meters, depending on the complexity of the terrain. About 910,000 observations from the ATL08 data were compared against LiDAR data over a forested area in Finland to achieve an overall vertical error for the terrain of RMSE <0.73 m (Neuenschwander et al. 2020). However, another study compared the RISAT-1 stereo radargrammetry DEM elevations against the ATL08 elevations as well as GPS points and found that the RMSE difference between the ATL08 and the GPS points was about 40 m (Saini, Bhardwaj, and Chatterjee 2019). Some factors may contribute to enhancing or degrading the vertical accuracy of the ATL08 product, such as weak or strong beam energy, the time of data collection-either nighttime or daytime, and vegetation density. Hence, the use of weak energy beam data should be avoided in forested areas and areas with complex topography (Zhu et al. 2020). Also, daytime datasets may have more noise than nighttime data, which decreases the accuracy of the surface finding processes (Popescu et al. 2018). In 2020, Liu et al., have used the ATL08 product to evaluate some global DEMs with different resolutions (Liu, Popescu, and Malambo 2020). However, they neglected the effect of the terrain aspect, slope, and land cover on the ATL08 heights and height uncertainty.

The existing research discussed in this section evaluated the accuracy of the ATL08-terrain product under a variety of topographic and vegetation conditions. However, it does not fully explain how this product can be used to evaluate other elevation products. Additionally, these researchers have not adequately addressed the issue of filtering the ATL08 terrain data, especially in mountainous areas with complex terrain. Nor have they suggested any methods to minimize the resulting errors in order to improve the accuracy of the ATL08-Terrain product. Hence, our study aims to fill this gap and assess the accuracy of the ATL08 terrain product over a forested rough topography using a high-resolution LiDAR DTM. We also compared the accuracy of the latest versions of different elevation datasets (i.e. ASTER, SRTM, and TDX DEMs) evaluated by the ATL08 strong beams, weak beams, and all beams versus the accuracy evaluated by the LiDAR DTM alone. Furthermore, we studied the effect of land cover types, terrain aspect, and terrain slope on the vertical sampling error and height uncertainty of the ATL08 strong and weak beams. We also present a simple yet effective uncertainty-based filtering method to increase the absolute vertical accuracy of the ATL08 terrain product.

This paper is organized in the following manner: Section 2 describes the topographic characteristics of the study area, section 3 covers the datasets used for this experiment, section 4 describes in detail the methods of processing, assessment, and enhancement of the ATL08-Terrain product and the other datasets. The results are presented in section 5 with a comprehensive analysis and discussion while highlighting the significance and improvements presented in our study. In the last section, we summarized the conclusions.

2. Study area

The Kaibab Plateau lies in Coconino County, northern Arizona USA. The study area is in the middle part of the Kaibab Plateau between the latitudes (36.4299°–36.5924° N) and the longitudes (112.0640°–112.4007° W), with dimensions of (17.362 km × 27.673 km). The total area is about 480.5km^2, as shown in Figure 1. The Kaibab Plateau is bounded by a red polygon and the study area is bounded by a cyan rectangle.

The region has a complex topography with hilly (2° –6°), and steep mountain (6°–25°) Slopes. While portions of the land slope downward on a gentler grade, there are several portions that lie in high mountain areas with slopes that exceed 25°. The elevations range between 1963 m and 2802 m above the North American Vertical Datum of 1988 (NAVD 88). The land is fully vegetated with variegated forests, plants, and grass; but evergreen forests are the dominant land cover type in this area.

3. Datasets

There were three kinds of data used in this study. First, satellite-derived elevation data were used to measure the terrain heights. Second, validation data that have high quality and high precision elevations with a centimeter level accuracy were used to assess the vertical accuracy of the measured heights. Third, Land Use Land Cover data (LULC) were used to study the effect of the different land forms on the measured heights and the height errors.

3.1. Elevation data

The Elevation data are the ICESat-2 ATL08 product V3, ASTER DEM V3, SRTM DEM V3, and the TanDEM-X DEM V1. The information related to the resolution, version release, and download websites are listed in Table 1.

The ATL08 data, ASTER DEM, SRTM DEM are provided by the National Aeronautics and Space Administration. While, the TDX DEM is provided by the German Aerospace Center (DLR). The ASTER DEM version 3 and the ATL08 data version 3 were newly released in 2019 and 2020, respectively. Therefore, a few studies had the opportunity to assess their accuracy and discover potential errors in them. There is only one version of TDX at 90 m resolution released in 2016 and there have been no versions released after that so far. The SRTM V3 is latest version of DEM at 30 m resolutions. There are version 4 and version 4.1 released by CGIAR Consortium for Spatial Information (CGIAR-CSI). However, these versions are at 90 m resolution.

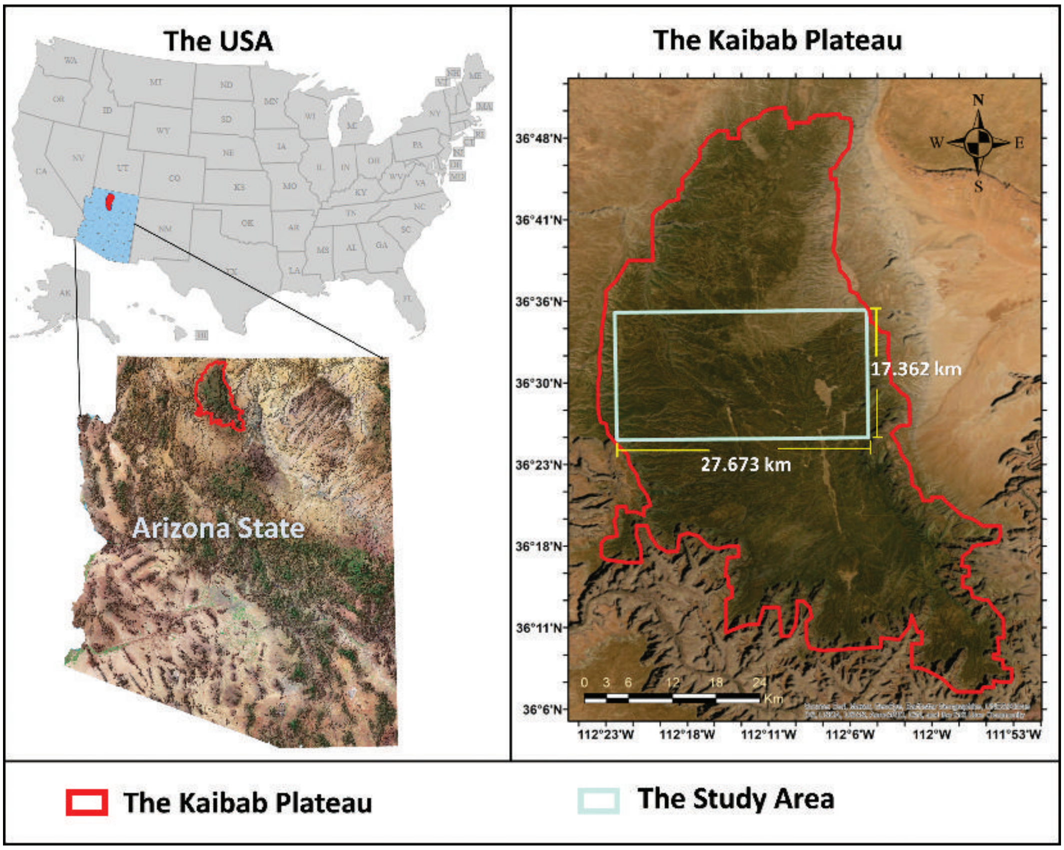

Figure 1. The Kaibab Plateau, Arizona, USA.

Table 1. ICESat-2/ATL08, ASTER, SRTM, and TDX elevation data products for the Kaibab Plateau, Arizona, USA.

Product	Version	Spatial resolution	Download website
ATL08	V3 (2020 release)	100 m interval in along-track direction	https://search.earthdata.nasa.gov/search/
ASTER	V3 (2019 release)	30 m	https://search.earthdata.nasa.gov/search/
SRTM	V3 (2014 release)	30 m	https://dwtkns.com/srtm30m/ https://search.earthdata.nasa.gov/search/
TDX	V1 (2016 release)	90 m	https://download.geoservice.dlr.de/TDM90/

3.1.1. The ICESat-2/ATL08 V3

The ATL08 product consists of two classes, one for the terrain elevations above the WGS 84 ellipsoid and the other for the canopy relative elevations. The elevations in this product were created by dividing the corresponding ground track in the ATL03 product into smaller segments (10 km long). Each segment was separately processed to filter the data and obtain the terrain and canopy surfaces (Neuenschwander et al. 2019). The results of the surface finding algorithm are a 100 m segment of terrain elevations, and fewer and sparser canopy elevations. There may be some missing terrain and canopy observations in the ATL08 products due to the low density of the photon backscatters and the performance of the filtration algorithm. The relevant information about the ATL08 beams is listed in Table 2.

Since we need to study the possibility of using both the strong and weak beams as reference data to evaluate the global DEMs which have a wider spatial coverage than a single ICESat-2 ground track, we selected all the available strong and weak beams over the area of interest. Therefore, a total of 50 strong and weak beams (25 strong and 25 weak) were used separately and together for evaluating the DEMs. Also, the effect of the terrain aspect, slope and land cover was separately investigated for each of them.

3.1.2. ASTER GDEM V3

The Terra Advanced Spaceborne Thermal Emission and Reflection Radiometer Global DEM (ASTER GDEM) is a photogrammetric DEM based on stereo Near-Infrared (NIR) images covering the area between 83° N and 83° S (Ravibabu et al. 2010). The first version was released in 2009 at a 30 m resolution (1 arcsec); however, it was not at the same quality as SRTM (3 arcsec) (Guth 2010). The second version was enhanced and released in 2011. This version contains some anomalies and features that could result in significant errors in small areas (Arefi and Reinartz 2011). The third version was corrected for cloud effects and the outliers were removed using other reference DEMs. This version was also corrected for the elevations of the water bodies. Therefore, a separated global product for water bodies (ASTWDB) was created (Abrams, Crippen, and Fujisada 2020). The elevations in all versions were referenced to the Earth Gravitational Model (EGM 96) as a vertical datum (Zhang et al. 2021).

Table 2. ICESat-2/ATL08 ground tracks over the study area in the Kaibab Plateau, Arizona, USA.

GRANULE DATE	GROUND TRACK	NO OF STRONG & WEAK BEAMS
2019-01-02	1R, 1L, 2R, 2L, 3R, 3L	3 strong & 3 weak
2019-10-01	1R,1L,2R,2L	2 strong & 2 weak
2019-12-31	1R, 1L, 2R, 2L, 3R, 3L	3 strong & 3 weak
2020-01-29	2R, 2L, 3R, 3L	2 strong & 2 weak
2020-03-31	1R, 1L, 2R, 2L, 3R, 3L	3 strong & 3 weak
2020-06-30	1R, 1L, 2R, 2L, 3R, 3L	3 strong & 3 weak
2020-07-29	3R, 3L	1 strong & 1 weak
2020-09-29	1R, 1L, 2R, 2L, 3R, 3L	3 strong & 3 weak
2021-03-06	2R, 2L, 3R, 3L	2 strong & 2 weak
2021-03-29	1R, 1L, 2R, 2L, 3R, 3L	3 strong & 3 weak
TOTAL	50 ground tracks	25 strong beams & 25 weak beams

3.1.3. SRTM DEM V3

The Shuttle Radar Topography Mission (SRTM) DEM is a radar interferometry-based DEM released in 2002 to measure the Earth's topography above the mean sea level as determined by the EGM 96. The DEM measurements cover 80% of the Earth for the regions between the latitude of 60° N and 54° S. The first version was made at 30 m resolution (1 arcsec) for the USA and 90 m resolution (3 arcsec) for other regions of the world. In this version, radar echoes were transformed into DEM strips and a mosaic was created at $1° \times 1°$ (Farr and Kobrick 2000). In the second version, the water bodies and coastlines were defined, and spikes and wells were removed by interpolation methods (Slater et al. 2006). The SRTM v3 or SRTM plus is a void-filled version in which the interferometric methods were enhanced to eliminate the gaps in the data, especially over steep mountainous areas like the Himalayas or over desert areas which have no reflections. Other national and global DEMs were used to fill the voids in this version such as ASTER GDEM v2, USGS Global Multi-resolution Terrain Elevation Data (GMTED) and USGS national datasets (NASA 2015).

3.1.4. TDX DEM V1

The TanDEM-X DEM is a radar interferometry-based DEM built from the measurements captured by the TanDEM-x and TerraSAR-X satellites from 2010 to 2015 and cover the whole globe (Dong et al. 2021; Bangen 2013). There is only one available global version of this DEM. It contains many voids, artifacts, outliers, and noise in water bodies, rugged terrain, and in high vegetation cover (Hueso González et al. 2010). The measurements were not processed to detect the bare-ground elevations; therefore, this version is a digital surface model (DSM). The elevations values were sampled at a 90 m resolution and were referenced to the vertical datum (WGS 84 ellipsoid). There are 12 m and 30 m resolution DEMs available for scientific use at (https://tandemx-science.dlr.de) for a limited area of 10,000 km^2.

3.2. Land cover data

The National Land Cover Database 2019 (NLCD) is the latest land cover product release provided by the U.S. Geological Survey for the USA. The product was generated from the 30 m resolution LandSat images with an epoch of two to three years. It contains 34 classes for the land cover, urban and vegetations based on the modified Anderson Level II classification system. The land cover classifications for years 2001, 2004, 2006, 2008, 2011, 2013, 2016, and 2019 are available within the NLCD 2019 dataset and can be downloaded through the Multi-Resolution Land Characteristics (MRLC) Consortium (https://www.mrlc.gov/data).

3.3. Validation data

The validation dataset was an airborne LiDAR-based DTM, collected in September 2012. The DTM has a 1 m spatial resolution and a vertical accuracy of RMSE ≤15 cm. The DTM horizontal coordinate system is UTM Zone 12N [EPSG: 26,912], the vertical coordinate system is the NAVD88 datum [EPSG: 5703]. The measurements were referenced to the North American Datum of 1983 (NAD 83). The data was collected by 3Di West and was made available on the open topography website which provides high-resolution topographic data such as raster, point cloud, and image differencing currently accessible from the USGS, some universities, data centers, and scientific programs in the USA. The data was downloaded through (https://doi.org/10.5069/G9TX3CH3).

4. Methods

The spatial coverage of ATLAS ground tracks is quite different from that of ASTER, SRTM, and TDX DEMs since they are based on satellite images with a wider spatial coverage. In order to evaluate and compare the ATL08 height data with ASTER, SRTM and TDX DEMs, the steps in Figure 2 were followed.

Figure 2 illustrates the general steps for using the LiDAR DTM as reference data to assess the ICESat-2/ATL08, ASTER, SRTM, TDX DEMs while investigating the impacts of terrain aspects, slope, and land cover types on their accuracy. The slope, aspect and height maps were generated from the Lidar DTM. The ATL08 ground tracks were filtered using the height uncertainty values associated with each ATL08-Terrain observation. The ATL08 filtered observations were matched to the slope, aspect, and Lidar elevation maps as well as the ASTER, SRTM, and TDX DEMs to extract the corresponding slope, aspect, and heights. Since the elevations in this study have different vertical and horizontal datums, datum unification was applied for comparison matters. Finally, the Lidar DTM as well as the ATL08-terrain elevations were used to assess the ASTER, SRTM, and TDX DEMs.

4.1. Creating aspect, slope, contour and land cover maps

The LiDAR DTM with a 1 m resolution and <15 cm accuracy, was utilized to generate slope, aspect, and contour maps to analyze the topography of the study area. The slopes were divided into four classes: flat to gentle slope <2°, hilly slope 2° – 6°, mountain area 6° – 25°, and high mountain area >25°. The aspect of the terrain was divided according to the primary and the secondary directions into nine classes: flat, North, Northeast, East, Southeast, South, Southwest, West, and Northwest. The contour map heights were divided into five classes with a contour interval of 50 m.

The land cover data was downloaded and cropped to the study area to create a land cover map. We reclassified and combined the same sub-classes into higher-level categories. Thus, high intensity urban area, low intensity urban area, etc., were grouped into the urban area class. The final land cover map contained eight classes.

4.2. The ATL08 processing

We downloaded the ATL08 ground tracks over the study area as mentioned in section (3.1.1.) and cropped the tracks to the desired latitude and longitude. We also classified the ATL08 ground tracks into strong beams and weak beams, and extracted the terrain heights and height uncertainty from both. Height uncertainty is the only factor associated with the ATL08 product that expresses the vertical sampling precision. This term can be calculated by adding the errors from the height measurements plus the errors of the measurement process (Neuenschwander and Magruder 2016). We examined many thresholds starting from 100 m and below. Each time, we assessed the accuracy of the ATL08 terrain heights at the chosen threshold. We found that the ATL08 accuracy does not exhibit a significant enhancement in accuracy from the 5 m to 20 m thresholds. However, most of the data points were removed as the threshold decreased. Therefore, we removed all the observations which had uncertainty values >20 m in order to eliminate the imprecise terrain observations.

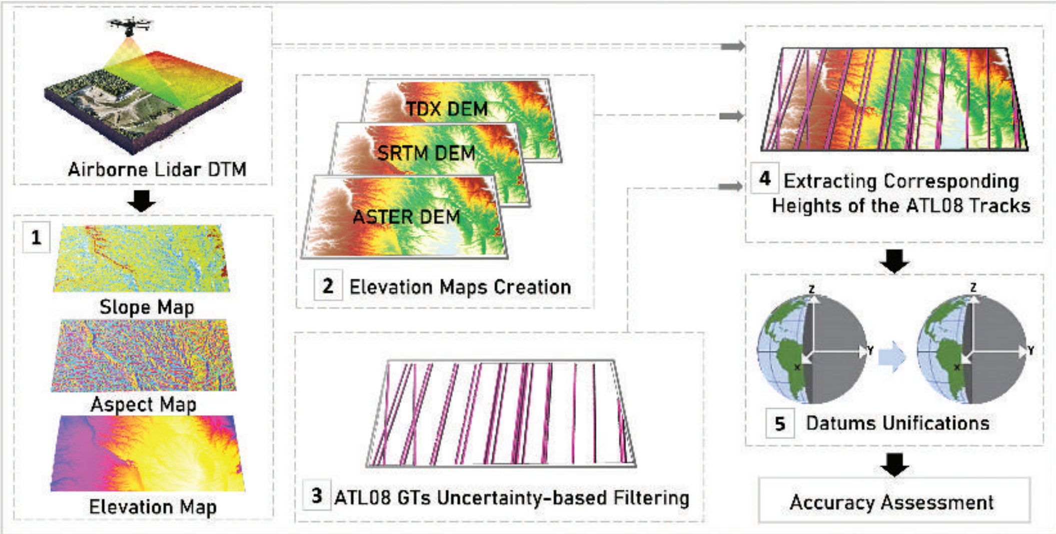

Figure 2. Schematic flowchart of the general method used for data processing and assessment.

4.3. Extracting the ATL08 ground tracks corresponding information

The ASTER, SRTM and TDX DEMs were downloaded and cropped to the desired areas using the Geographic Information System software (GIS software). The geographic latitude and longitude of the ATL08 strong and weak beams were matched with the ASTER, SRTM, and TDX DEMs to extract the corresponding elevations for the ground track locations. The slope, aspect, and land cover information were extracted to the ATL08 strong and weak beams by "Extract Multi Values to Points" Function.

4.4. Datums and coordinates systems transformation

Since the ATL08 heights are related to WGS 84 ellipsoid and the other data are related to different datum as shown in Table 3. All datasets were converted into the same coordinate system and the same vertical datum relative to the WGS84 ellipsoid.

The ASTER and SRTM DEM elevations were directly converted from the EGM96 geoid to the WGS84 ellipsoid through the equation

$$H = H_o + N \tag{1}$$

where H is the ellipsoidal height, H_o is the orthometric height, and N is the geoid undulation.

Table 3. Coordinates system and datum transformation for the datasets.

Data	Horizontal Datum	Vertical Datum
Lidar_ DTM	NAD 83	NAVD88 [EPSG: 5703]
ATL08	WGS 84	WGS 84 Ellipsoid
ASTER	WGS 84	EGM 96 GEOID
SRTM	WGS 84	EGM 96 GEOID
TDX	WGS 84 (G1150)	WGS 84 Ellipsoid

The Kaibab Plateau DTM LiDAR observations were referenced to the NAD 83 as a horizontal reference frame while NAVD 88 was taken as the vertical reference frame. To evaluate the global DEMs with the observation taken by the airborne LiDAR DTM, the LiDAR DTM observations were converted into the WGS 84 ellipsoid by the NOAA/NOS's VDatum 4.2 available at: (https://vdatum.noaa.gov/) to unify the vertical datum.

4.5. DEMs assessment using the ATL08 strong and weak beams

The performance of the ATL08 strong and weak beams was evaluated in two steps. In the first step, we evaluated the ATL08 strong beams with the LiDAR DTM heights extracted at the locations of the strong beams. We evaluated the ATL08 weak beams in the same way, with the LiDAR DTM heights extracted at the locations of the weak beams. In the second step, we created 10 thousand random points over the entire area and evaluated the accuracy of the ASTER, SRTM, TDX DEMs at these points with LiDAR DTM. Subsequently, we compared the results from the second step with results from the first step. This evaluation was done based on the Standard Deviations (STD), the Root Mean Square Error (RMSE), and the Mean Absolute Error (MAE), which were calculated according to the following equations:

$$RMSE = \sqrt{\frac{\sum_{i=1}^{n} \left(X_{Valid_i} - X_{DEM_i}\right)^2}{n}} \tag{2}$$

$$STD = \sqrt{\frac{\sum_{i=1}^{n} \left|X_{DEM_i} - X_{mean}\right|^2}{n-1}} \tag{3}$$

$$MAE = \frac{1}{n}\sum_{i=1}^{n} |X_{DEM_i} - X_{Valid}| \quad (4)$$

where X_{DEM} is the elevation values of the DEM, n is the number of the observations, X_{mean} is the mean value of the DEM elevations, and X_{Valid} is the elevations of the validation data.

5. Results & discussion

5.1. Terrain analysis maps

The aspect, slope, contour, and elevation maps in Figure 3 show the topographic changes in the Kaibab Plateau. The slope map indicates the steepness of the terrain, while the terrain aspect map indicates the directions of the terrain slopes. The height maps indicate the different terrain elevations. Figure 3(a) illustrates the slopes where there are almost no flat areas (<2°) and the mountainous slopes (6° – 25°) dominate most of the region. There are some steep slopes located in the high mountain areas (>25°) on the left side and on the bottom right side. Figure 3(b) shows that the right part of the area slopes toward the east, the left part slopes toward the northwest, and the entire study area slopes slightly to the north direction.

In Figure 3(c,d), the elevation values of the eastern part are generally higher than the western part of the area and the highest values lie in the southeast of the study area where the peak of the Kaibab mountain exists. The 839 m height difference between the highest and the lowest elevations in only 480.5 km^2 reveals the mountainous nature of the land and the extreme gradient in elevations in the region.

The land cover map was generated from the NLCD 2019 data. Figure 4 shows the eight land cover types within the area frame. Table 4 illustrates their definitions and the percentage of coverage for each class with respect to the total coverage.

Most of the area is covered by the green color which represents the evergreen forests (75.05% of total coverage) where there are different species of trees more than 5 m tall. What distinguishes the evergreen forest is that approximately 75% of its trees retain their leaves throughout the year. This can prevent ATLAS photons from penetrating the vegetation cover at any time of the year to provide an accurate shape of the surface of the earth in densely vegetated areas. The urban area in the white color is only 0.41% of the total coverage and the other classes like mixed forests and woody wetland represent very small parts of the area (0.02% and 0.001%), respectively. Therefore, it is quite hard to recognize them from the map.

Figure 4 also shows the ATL08 strong beams (the lines in black) and the ATL08 weak beams (the lines in magenta). Most of the tracks lie in the evergreen forests, shrub land, and grass land and only very few tracks pass through the urban areas. The count of the ATL08 observations in each class and the percentage of the total observations are listed in Table 5.

In Table 5, after filtering the observations with uncertainty >20 m, the total number of the observations of the strong beams was about four times the total number of the observations of the weak beams. In general, the percentage of the ATL08 observations in a particular land cover is directly proportional to the percentage of this land cover

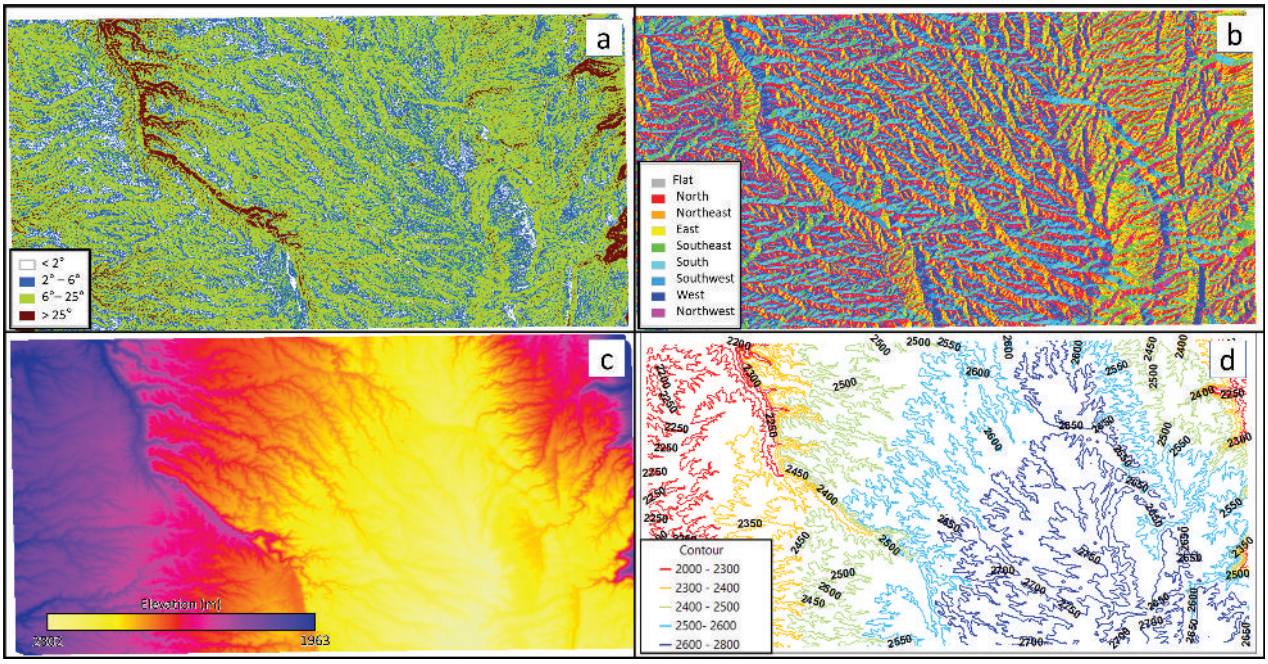

Figure 3. Terrain analysis of the study area (a) slope map, (b) Aspect map, (c) Elevation map, and (d) contour map.

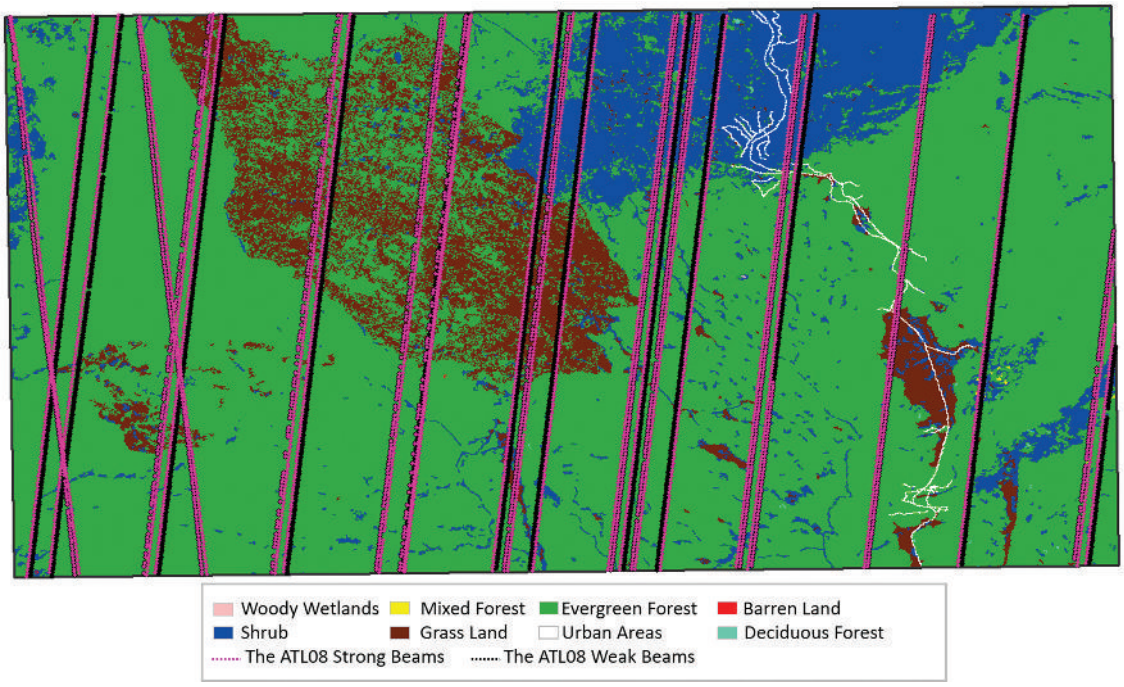

Figure 4. Land cover map for the study area in the Kaibab Plateau, Arizona, USA. (The black lines represent the ICESat-2/ATL08 strong beams and the magenta lines represent the ICESat-2/ATL08 weak beams).

Table 4. The description of the land cover classes in the Kaibab Plateau, Arizona.

Land Cover Class	Definition	% of the area land cover
Woody wetlands	• Contain forest or shrubland • Canopy density > 20% of total cover • Soil is periodically covered with water	0.001%
shrub	• Young trees < 5m tall • Canopy density >20% of total cover	13.44%
Mixed forest	• Trees > 5m tall • Canopy density > 20% of total cover • Mix of deciduous &evergreen species	0.02%
Grass	• Herbaceous flowering plants like sedges and forbs • Canopy density > 80% of total cover	11.0%
Evergreen forest	• Trees > 5m tall • Canopy density > 20%of total cover • 75% of trees maintain their leaves all the year	75.05%
Urban areas	• Mixture of constructions and vegetations • Canopy density <20% of total cover	0.41%
Deciduous forest	• Trees > 5m tall • Canopy density >20%of total cover • 75% of trees maintain their leaves all the year	0.04%
Barren Land	• Mixture of rocks, sand, clay, volcanic materials and other earthen materials • Canopy density < 15% of total cover.	0.003%

with respect to the total area. Therefore, most of the observations of the strong and weak beams fall in the evergreen forests. The urban areas, deciduous forests and barren land were subject to very few observations for both strong and weak beams. Therefore, we excluded these classes from our analysis.

5.2. The relationship between height uncertainty and the ATL08 terrain errors

Height uncertainty reflects the error in the ATL08 product and is a measure of the precision of the vertical sampling and the potential height uncertainty (Neuenschwander and Magruder 2016). The inherent quality of the output from the ATL08 algorithm combined with solar noise; raise the uncertainty in the derived terrain and canopy products (Magruder and Brunt 2018). In our study, we found very high values for height uncertainty for the ATL08 weak beams (>800 m) and strong beams (>200 m). Thus, if we want to use the ATL08 as a height reference, it is necessary to remove the imprecise elevation measurements.

For simplicity in this discussion, we will now express the ATL08 strong beams with the term ATL08_s and the weak beams with the term ATL08_w. As we classified the ATL08 ground tracks into strong and weak beams the observations with the height uncertainty of more than 20 m were removed

Table 5. Land cover classification of the filtered ATL08 strong and weak beams observations over the Kaibab Plateau.

Beam / LULC	ATL08 Strong Beams		ATL08 Weak Beams	
	Count	%	Count	%
Woody wetlands	-		-	
Shrub	445	17.57	149	24.34
Mixed forest	91	3.59	31	5.07
Grass land	206	8.13	50	8.17
Evergreen forest	1785	70.47	382	62.42
Urban areas	1	0.04	-	-
Deciduous forest	2	0.08	-	-
Barren Land	3	0.12	-	-
Total observations	2533	100%	612	100%

from the ATL08_S and ATL08_W. Figures 5 and 6 show the relationship between height uncertainty and the ATL08 residuals. The residuals were classified according to density distribution, aspect, slope, and land cover before the observations with uncertainty >20 m were removed and depicted in Figure 5. Figure 6 shows density distribution, aspect, slope, and land cover after observations with uncertainty >20 m were removed. Panels 5 (a), 5 (b), 5 (c), and 5 (d) refer to the ATL08_s, while panels 5 (e), 5 (f), 5 (g), and 5 (h) refer to the ATL08_w.

Figure 5 shows the original ATL08 strong and weak beams height errors against the height uncertainty. In Figures 5(a–d), the uncertainty values for the strong beams were <300 m and the height residuals are between −15 m and 15 m and in Figures 5 (e–h), the uncertainty values for the weak beams are >800 m and the height residuals are between - 10 m and 20 m. this indicates that the weak beams contain higher levels of uncertainty, and consequently, higher values of errors. In Figure 5(a), based on the density plot we can see that below the 50 m uncertainty, the ATL08_S residuals are limited between (−8 m to 8 m), and above the 50 m uncertainty, some residuals exceed 12 m. According to aspect classification Figure 5(b), it is difficult to detect any pattern that relates the occurrence of errors to the aspect of the terrain. In Figure 5(d), the highest values of the errors lie in the high mountain and mountain areas with slopes >25° and slopes range between 6° and 25 °, while the flat and the hilly slopes <6° have the minimum residuals. In Figure 5(c), most of the high residual values lie in the evergreen forests and some high values lie in the shrub land which has small trees <5 m tall. However, if we compare the same points in Figure 5(c–d), we can see that the points that lie in the shrub land and have a high residual it also has a very steep slope and lie in a high mountain area. Therefore, it is difficult to separate the effect of the land cover from the effect of the slope over the terrain residuals. But based on Figure 5, we can infer that the denser the vegetation and the steeper the land, the higher residuals the ATL08 will has.

In Figure 5(e), the density plot for the weak beams shows that most of the observations lie below the 200 m uncertainty; however, it is hard to distinguish the detailed relationship between the uncertainty and the residuals in this area, due to the high uncertainty in the weak beams (>800 m). Despite that, from this figure we can generally observe a positive relationship between the uncertainty and ATL08 errors. Again, in Figure 5(f), we could not link the height errors in the weak beams to the terrain aspect, as in the case of strong beams. In Figure 5(h), the highest values of error lie in the mountain areas with slopes and the high mountain slopes. The hilly slopes have lower residuals than the mountain slopes (6°– 25°), however, we can find a point with a gentle slope which has an error value of −5 m. If we compare the same point with the land cover classification in Figure 5(g), we can see that this point lies in the evergreen forests which have trees >5 m tall. Therefore, this confirms our assumption that the slope effect cannot be completely separated from the land cover effect. Figure 6 shows the ATL08 strong and weak beams after removing the points that have uncertainty levels more than 20 m. panels 6 (a), 6 (b), 6 (c), and 6 (d) refer to the ATL08_s, while panels 6 (e), 6 (f), 6 (g), and 6 (h) refer to the ATL08_w.

In Figure 6(a), the residual values were decreased to (−4 m to <5 m) in strong beams. The highest value of error exists in the uncertainty between (15 m – 20 m). Below the 5 m uncertainty, the errors are limited to (−2 m – 2 m). However, we could not remove the observations of uncertainty <5 m because a huge amount of data will be lost if those observations were removed. In Figure 6(d), most of the residuals lie in the slopes >25 ° and the slopes (6°– 25°), and the flat, gentle and hilly slopes have the lowest values of residuals. In Figure 6(c), the highest residual lies in the evergreen forest. However, the land cover effect cannot be distinguished anymore below an uncertainty of 7 m, but it turns out that the slope has a stronger effect, and its influence can be differentiated even below this limit.

For the weak beams in Figure 6(e), the residual errors were limited to (−1.5 m – 1.5 m) with the uncertainty <20 m. Most of the errors for both the strong and weak beams are found in the negative direction, as shown in Figures 6(a–e). This indicates that the ATL08 overestimated the height values by about 0.5 m. In Figure 6(h), all the high mountain area slopes (>25°) for the weak beams were removed when the uncertainty became >20 m, still, the highest values of errors lie in the mountain areas with slopes (6°– 25°). The highest values of errors in Figure 6(g), are a mixture of evergreen forest and shrub land. The visual interpretation and comparison of Figures 5 and 6 illustrate that the errors in the ATL08_W

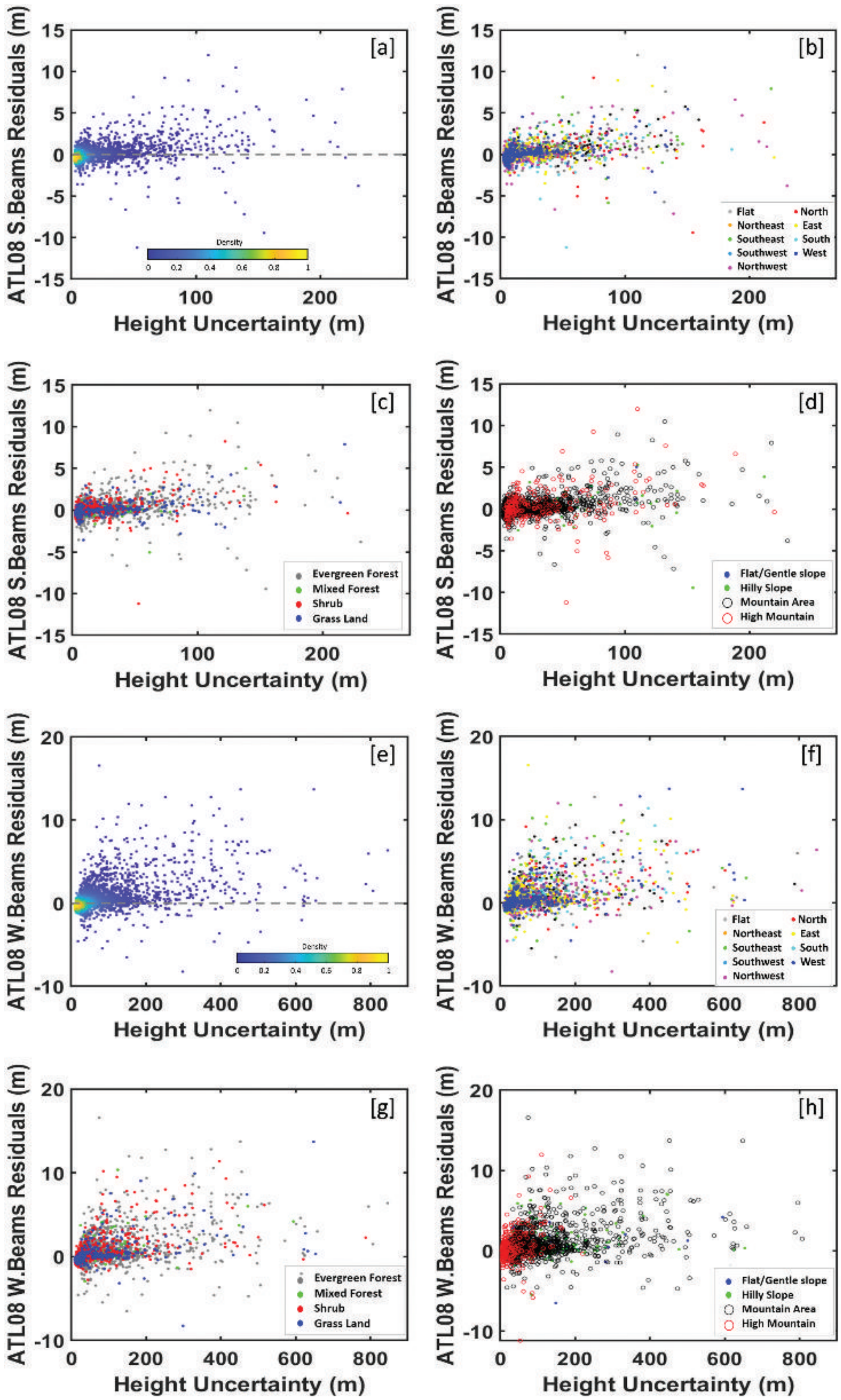

Figure 5. The relationship between height uncertainty and the ATL08 height residuals with error classification according to density, aspect, slope and land cover (before removing the observations with uncertainty > 20 m). Panels 5 (a), 5 (b), 5 (c), and 5 (d) for the ATL08 strong beams, and panels 5 (e), 5 (f), 5 (g), and 5 (h) for the ATL08 weak beams.

beams residuals were enhanced more than the ATL08_S beams when the uncertainty levels were reduced to <20 m, as shown in Table 6.

The evaluation of the strong and the weak beams in Table 6 was conducted using the DTM LiDAR elevations at the same ATL08_S and ATL08_W locations. The RMSE value for the original ATL08_S data was 1.036 m and the accuracy was enhanced to RMSE = 0.581 m after removing the uncertainty >20 m. Meanwhile, the accuracy of the ATL08_W was RMSE = 1.877 m; after enhancement, the RMSE decreased to 0.487 m. So, the accuracy of ATL08_S and ATL08_W were improved by

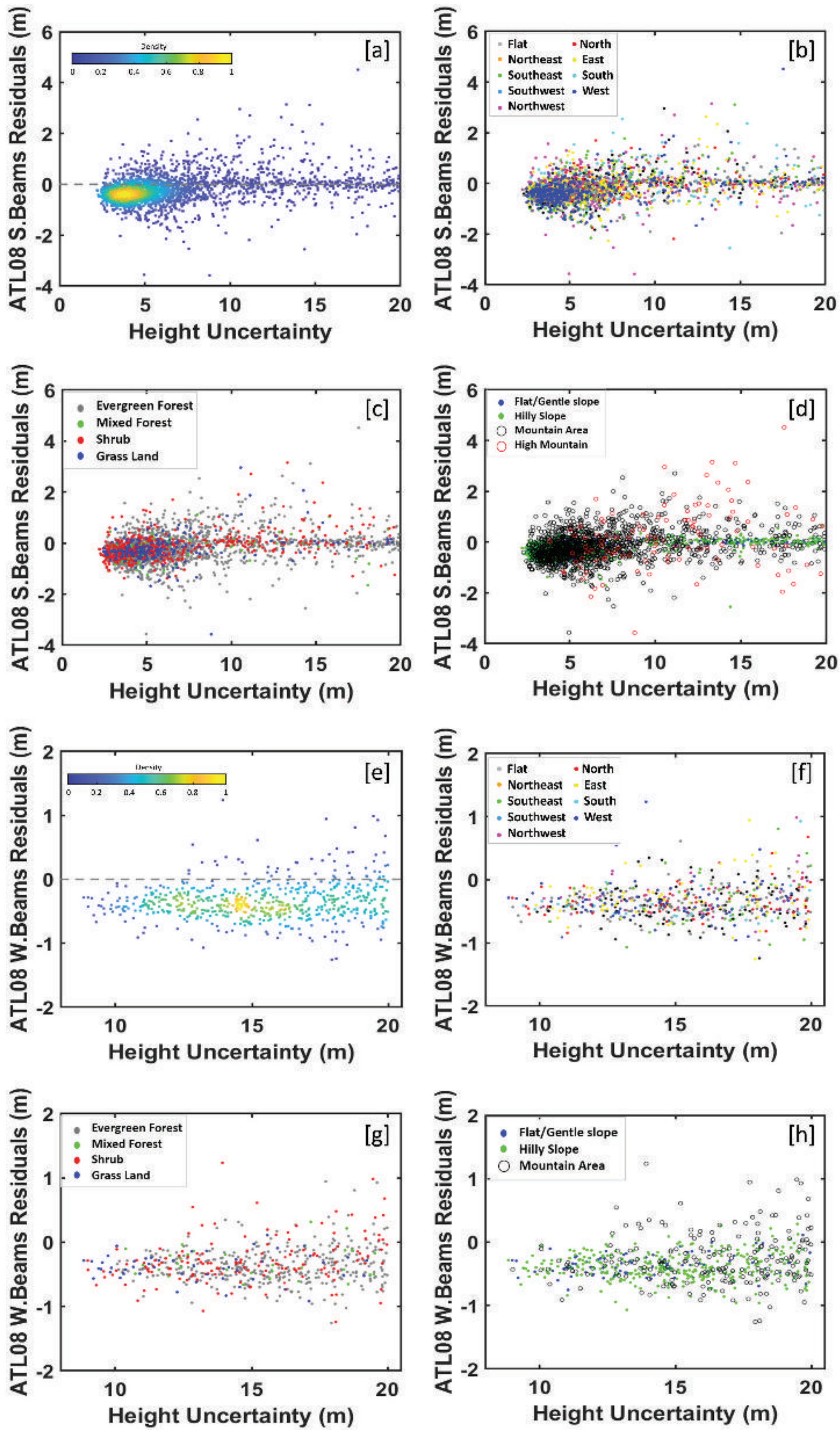

Figure 6. The relationship between height uncertainty and the ATL08 height residuals with error classification according to density, aspect, slope and land cover (after removing the observations with uncertainty > 20 m). Panels 6 (a), 6 (b), 6 (c), and 6 (d) for the ATL08 strong beams and panels 6 (e), 6 (f), 6 (g), and 6 (h) for the ATL08 weak beams.

0.455 m and 1.39 m, respectively. The mean absolute error value for both beams energy was also reduced. Table 7 presents descriptive statistics calculated for categories of terrain aspect, slope and land cover for the removed observations from the ATL08_S and ATL08_W terrain products.

According to Table 7, more observations were removed from the ATL08_W (2345 obs.) than the ATL08_S (930 obs.) which represent 79.30% of the original data for the weak beams and 26.85% of the strong beam's observations. The land cover classification for 66.23% and 68.91% of the removed data for

Table 6. The ATL08 strong and weak beams accuracy before and after removing the height uncertainty >20 m.

	Before removing uncertainty >20 m		After removing uncertainty >20 m	
	ATL08_S	ATL08_W	ATL08_S	ATL08_W
RMSE (m)	1.036	1.877	0.581	0.487
MAE (m)	0.582	0.582	0.435	0.435
STD (m)	144.585	145.125	148.570	133.110
Mean (m)	2487.189	2496.715	2501.558	2537.916
Median (m)	2512.651	2527.854	2546.946	2587.682

Table 7. Descriptive statistics for points with height uncertainty >20 removed from the ATL08_S and ATL08_W products.

Factor		ATL08_S (Strong Beams)	ATL08_W (Weak Beams)
Max uncertainty		230.50 m	846.21 m
Removed observation no.		930 observations	2345 observations
Percentage w.r.t. original obs.		26.85%	79.30%
LULC	Evergreen forest	66.23%	68.91%
	Mixed forest	2.79%	3.15%
	Shrub land	15.91%	17.95%
	Grassland	15.05%	9.50%
Slope	Flat to Gentle (<2°)	3.22%	4.98%
	Hilly (2°–6°)	15.80%	21.32%
	Mountain (6°–25°)	69.03%	66.78%
	High mountain (>25°)	11.93%	6.90%
Aspect	Flat	0%	0%
	North	10.75%	10.57%
	Northeast	14.08%	14.32%
	East	9.46%	10.44%
	Southeast	9.35%	9.08%
	South	16.02%	13.68%
	Southwest	16.02%	16.58%
	West	13.54%	13.09%
	Northwest	11.61%	12.91%

the strong and the weak beams lie in the evergreen forests followed by shrub lands then grasslands, and a very few of the observations lie in the mixed forests. We can attribute this phenomenon to the percentage of each land type with respect to the total land cover as discussed in section 5.1.1. Most of the removed observations fall in mountainous and hilly areas, as they are the most dominant slopes in the region. In addition, the removed points almost have similar values of aspect in all classes.

Our proposed method to improve the ATL08 accuracy based on the removal of the high uncertainty values >20 m delivered an increase of about 43% in the accuracy of strong beams and about 74% increase for weak beams. However, the proposed method reduced the number of strong beams observations from 3465 to 2533 as well as a significant decrease in the number of weak beams observations from 2957 to 612 observations. Our method yielded more accurate results than those of a former study by Carabajal and Boy, which used an ATL08 strong beam for ground heights retrieval and limited the terrain heights uncertainty to ≤7.5 m, however, they obtained an enhancement of only 16.17% for the strong beam (Carabajal and Boy 2020). We can attribute this to their use of the V3 of SRTM 90 m resolution model which probably has lower vertical accuracy than the ATL08 when evaluating the ATL08 product. In contrast, we used a 1 m spatial resolution LiDAR derived DTM with a vertical accuracy of (RMSE ≤15 cm) to evaluate the ATL08.

5.3. The impact of the terrain aspect, slope, and land cover on the DEMs error

Referring to the residuals of ASTER, SRTM, TDX DEMS, and ATL08 heights in the strong beams against the terrain aspect in Figure 7(a–d), and weak beams in Figure 7(e–h), we found that the aspect does not seem to have any effect on the ATL08_S and ATL08_W Figure 7(c, g). The aspect did have an effect however, on the other ASTER, SRTM, and TDX DEMs corresponding to the strong beams as they all show the same error trend. The errors lying in the regions from 0° to 180° are positively correlated, and the errors from 225° to 315° are negatively correlated. The errors for ASTER, SRTM and TDX DEMs corresponding to the weak beams are not correlated with the terrain aspect. This could be because the number of observations for the weak beams was much smaller than those from the strong beams to reveal this relationship.

Regarding the slope analysis for the different DEMs, Figure 8(c,g) show that the ATL08_S and ATL08_W residuals after removing the high uncertainty values are very low and the effect of the slope is minimal. However, we still can see some small deviations when the slope exceeds 25° in the strong beams in Figure 8(c). In the strong beams Figure 8(a–d), the ASTER, SRTM, and TDX DEMs have a negative correlation with the slope. This correlation decreased with the slope as the slope rose. Considering the weak beams observations illustrated in Figure 8(e–h), the slopes are generally <15° which indicates that the weak beams fall in gentler slopes than the strong beams.

Our results agree with previous investigations which found that the slope is the factor that has the greatest influence on the ATL08 terrain elevation accuracy as well as uncertainty (Wang et al. 2019; Yu et al. 2021; Tian and Shan 2021). We found that most of the removed observations (uncertainty >20 m) fall in steeply sloped areas ranging from mountain area slopes (6°–25°) to very steep slopes (>25°). All the high mountain area slopes >25° were completely removed from the ATL08 weak beams when we limited the uncertainty to <20 m, which indicates how slope degrades the accuracy of the ATL08 beams; especially, the weak beams. Our research shows that slope had almost had no effect on the ATL08 beams after removing the observations with high levels of uncertainty, unlike the ASTER, SRTM and TDX DEMs, which are strongly influenced by

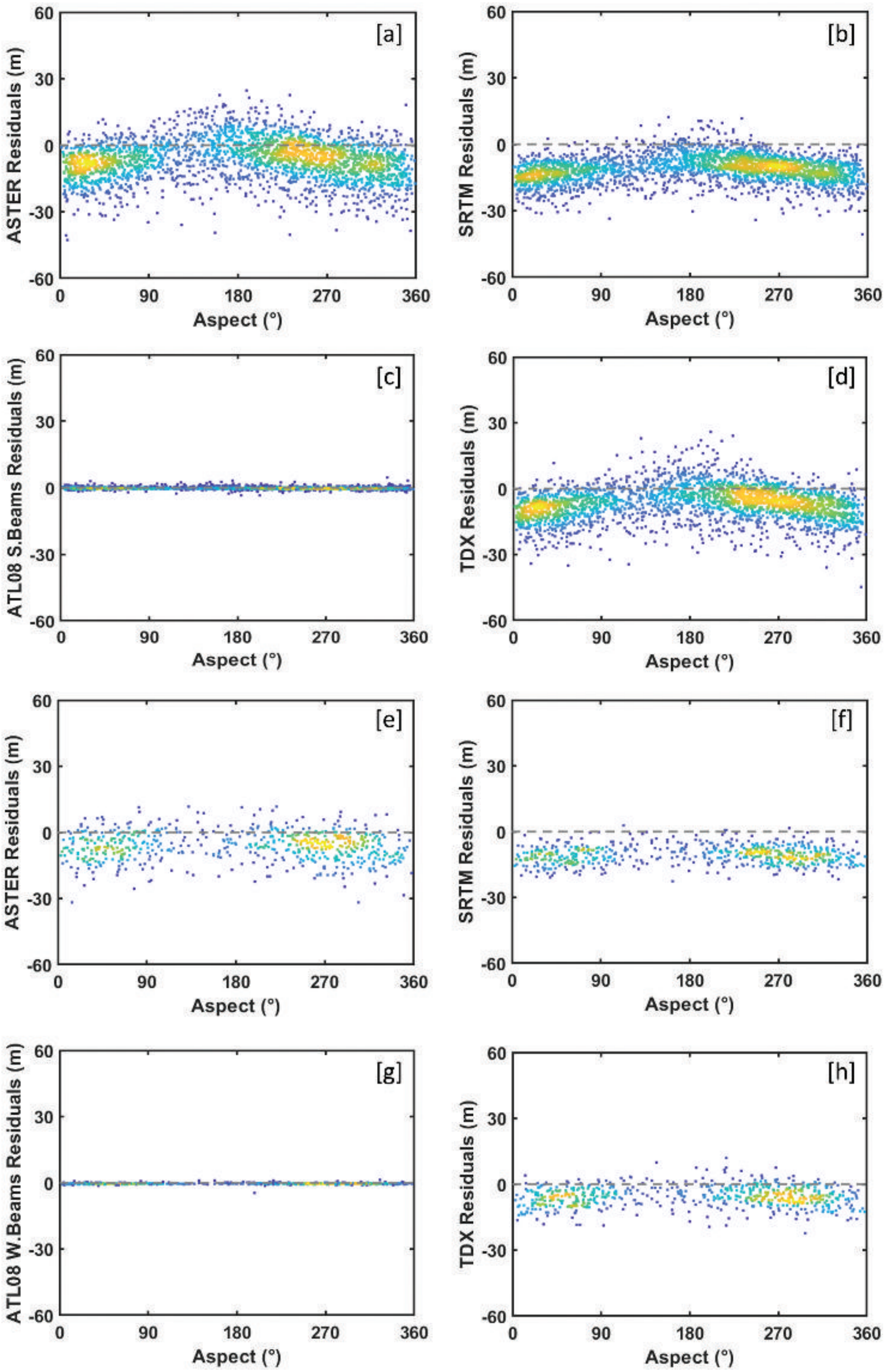

Figure 7. Aspect analysis for the ATL08 strong and weak beams and the corresponding ASTER, SRTM and TDX DEMs point locations. Panels 7 (a), 7 (b), 7 (c), and 7 (d) represent strong beams, whereas panels 7 (e), 7 (f), 7 (g), and 7 (h) represent weak beams.

slope. We should highlight that when we removed the ATL08 observations with uncertainty >20 m, the ASTER, SRTM, TDX and LiDAR DTM observations corresponding to the ATL08 removed points locations have been removed too, yet, we found some effects of slope and aspect on the other DEMs than on the ATL08 beams. These effects are due to the geometrical errors induced by these factors on the optical and SAR image processing, consequently, causing errors in the DEMs derived from these images.

The results in Figure 9 show that the DEM resolution does not have a major effect on DEM accuracy. However, we think that the novelty of the datasets, terrain roughness, the length, and density of the vegetation cover, may have higher effects on

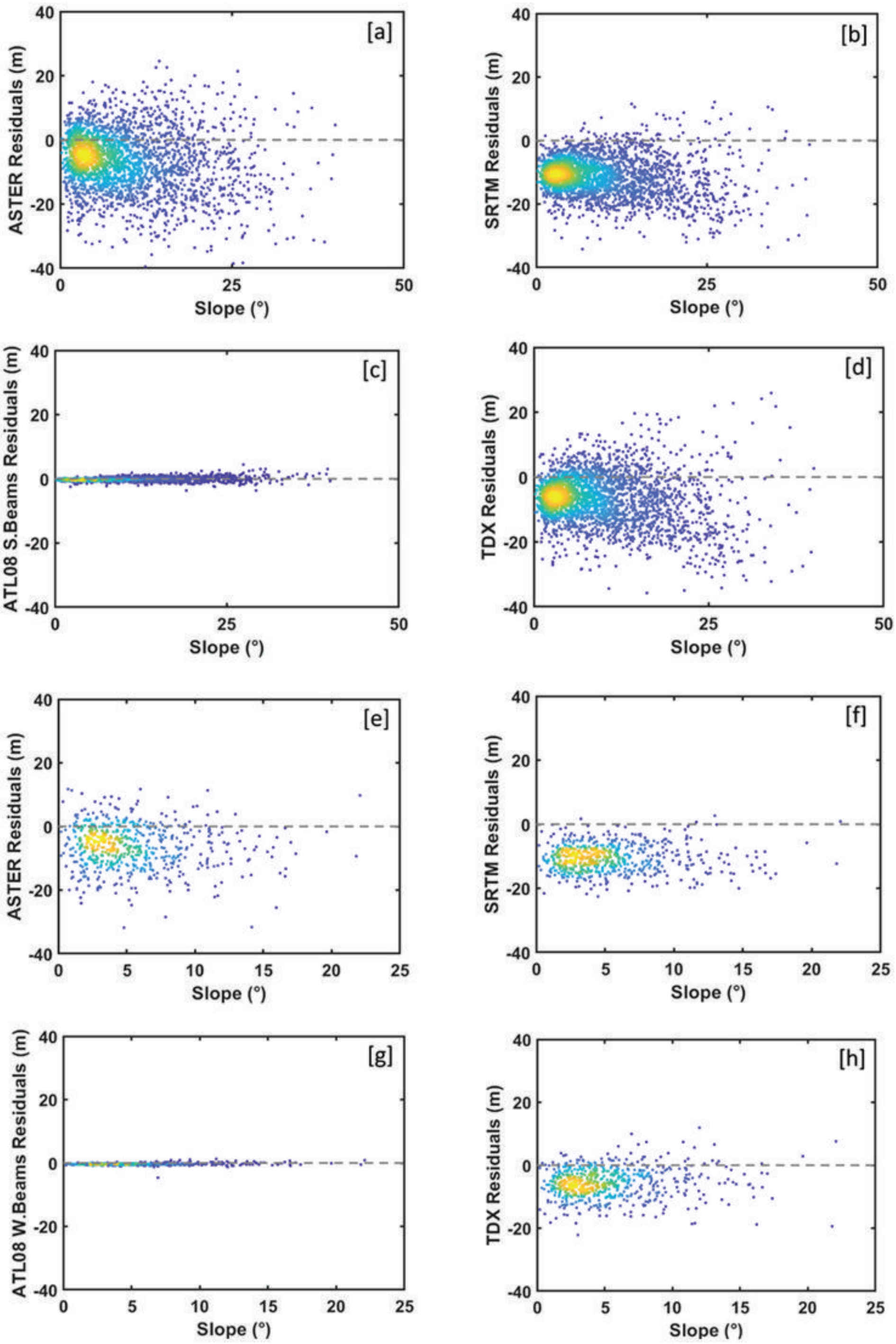

Figure 8. Slope analysis for the ATL08 weak beams and the corresponding ASTER, SRTM and TDX DEMs point locations.

the DEM quality. These conclusions can be observed by analyzing the values of the RMSE, MAE, and STD of the ATL08, ASTER, SRTM, and TDX DEMs over the different land types in the strong and weak beams.

For the strong beams, the 100 m resolution ATL08 was more accurate in terms of the RMSE than other DEMs overall land cover type. The 90 m resolution TDX DEM comes in the second place in terms of accuracy and shows a larger RMSE value over shrub land (C3) than over the other land cover types. The 30 m resolution ASTER DEM shows higher quality than the 30 m resolution SRTM overall land types. However, both DEMs have much lower accuracy than TDX DEM despite their higher resolution. All DEMs have MAE values very close to their RMSE, but the maximum mean error value occurred over the evergreen forests (C1) and the minimum mean error over the mixed forest (C2) for all DEMs except for TDX, which has the minimum mean absolute error over shrub land (C3). The STD

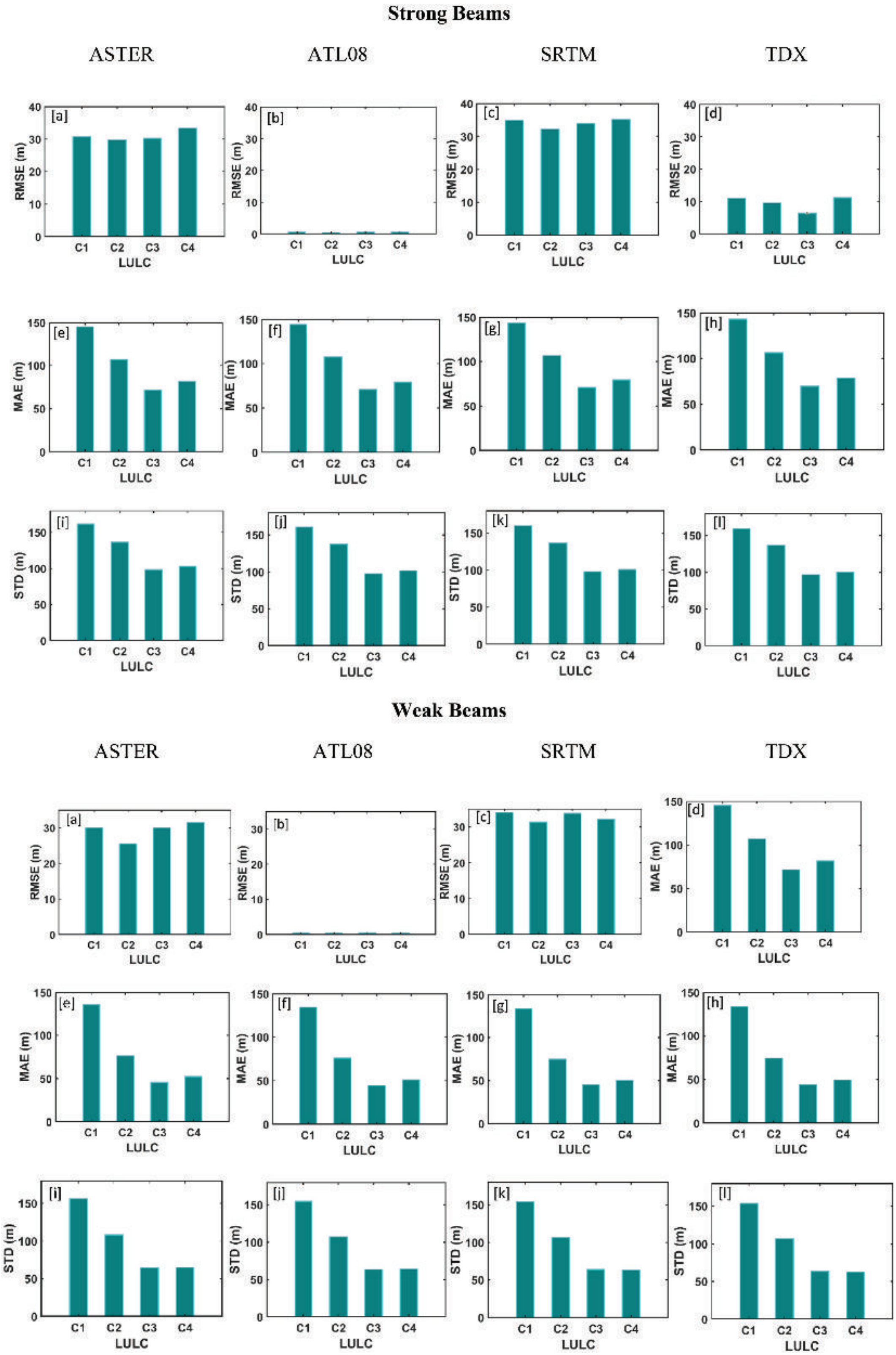

Figure 9. Error statistics to highlight the impact of the land cover on ASTER, SRTM, TDX DEMs and the ATL08 strong and weak beams. In the strong and weak beams, the top figures for the RMSE, the middle figures for the MAE, and the bottom figures for the STD. (C1= Evergreen forests, C2= Mixed forests, C3= Shrub land, and C4= Grass land).

values representing the roughness of the surface in different land cover (Asal 2019; Wu, Yang, and Li 2018), are nearly the same for all DEMs expressing the same trends over the various land cover types.

For the weak beams, the ATL08 also has the highest accuracy between DEMs. The SRTM shows a slightly better RMSE and MAE over the grass land (C4) than in the strong beams, and ASTER

DEM also shows a slightly better RMSE and MAE over the mixed forests (C2) than in the strong beams. The STD values show the same trend for all DEMs; however, they are generally lower than the STD values in the strong beams which show that the terrain is less rough than it was in the case of strong beams.

The land cover effect on the ATL08 strong and weak beams errors as shown in Figure 9 caused the maximum values of errors to exist in the evergreen forests where the densest vegetation cover and the trees >5 m tall (MAE = 0.45 m, RMSE = 0.59 m) for the strong beams and (MAE = 0.51 m, RMSE = 0.51 m) for the weak beams. The minimum error values however, fall in the mixed forests (MAE = 0.34 m, RMSE = 0.51 m) for the strong beams and (MAE = 0.39 m, RMSE = 0.38 m) for the weak beams. In contrast, the other global DEMs at higher resolution had an error range with a MAE <35 m, and an RMSE <35 m, for both strong and weak beams point locations. This indicates the sharp difference between the ATL08 accuracy and the accuracy of the other DEMs. Therefore, despite the higher spatial resolution of these DEMs, they cannot be used to evaluate the ATL08 terrain product over the same land cover types.

The presence of the vegetation in the scene adds more errors and noise mixed with the signal photons reflected from the vegetated terrain. As a result, it is difficult for the ATL08 algorithm to separate the signal and noise photons, especially when dealing with a very small number of reflected photons (Neuenschwander et al. 2019). Therefore, since we found that the ATL08 obtained good results over our study area, distinguished by complexity, hilly slopes, and dense and tall vegetation, we expect that it will have even better results over flatter terrain and low vegetated areas as previous studies obtained more accurate results over the flat terrain with gentle slopes than the rough terrain with steeper slopes (Dandabathula and Verma 2020; Zhu et al. 2020). However, in some cases, the presence of clouds may add more errors, thus undermining the accuracy of the ATL08 product.

5.4. Global DEMs assessment with the ATL08 strong and weak beams

As mentioned in Section 4.5.5, we performed two steps to assess the quality of the ATL08 strong and weak beams in evaluating the global DEMs. The first step results are listed in Table 8.

In Table 8, the 90 m resolution TDX DEM shows better accuracy (RMSE = 10.494 m) than the 30 m resolution ASTER and SRTM DEMs (RMSE = 11.683 m and 12.834 m, respectively) when they were evaluated by 10,000 points of LiDAR DTM randomly distributed all over the study area. The TDX and ASTER DEMs' mean elevations are very close to the ATL08 strong beams mean elevation listed in Table 6. The STD values for all DEMs are also closer to the ATL08 strong beams STD than the weak beams in Table 6. This shows that the ATL08 strong beams can better represent the terrain roughness than the weak beams due to their higher photon density.

In the second step, we evaluated the ASTER, SRTM, and TDX DEMs with (1) the ATL08 strong beams and corresponding LiDAR DTM points, (2) the ATL08 weak beams and the corresponding LiDAR DTM points, and (3) both the ATL08 strong and weak beams and the corresponding LiDAR DTM points. The results of the second step are listed in Table 9.

In Table 9, in case the strong beams, the differences between the DEMs accuracy (RMSE) assessed by the DTM LiDAR data and the ATL08 are very small <20 cm. These differences increase in case of the weak beams to become <35 cm. However, when we used both strong and weak beams together to assess the DEMs, the differences decreased again to <25 cm. When comparing the DEMs RMSE in Tables 8 and 9 to decide which set of ATL08 beams is the best to provide closest results of which have been obtained using a large number of points (10,000 points) distributed over the whole area, we found that the strong beams (in Table 9) have the closest results to the ones in Table 8 despite their fewer number of observations (2533 observations for the strong beams) with differences of (0.57 m, 0.208 m, and 0.353 m) for the ASTER, SRTM and TDX DEMs, respectively. The ATL08 weak beams in Table 9 with (612 observations), provided lower accuracies than the strong beams when they were compared with Table 8 with differences of (2.639 m, 1.72 m, and 3.393 m) for the ASTER, SRTM and TDX DEMs, respectively. The RMSE differences between Tables 8 and 9 were decreased again when the combination of strong and weak beams (with a total number of observations = 3145) have been used for the assessment with differences of (0.941 m, 0.488, and 0.869 m) for the ASTER, SRTM and TDX DEMs, respectively.

Further analysis was applied in order to check if there is a significant difference between the Lidar DTM and the ATL08-Terrain elevations. We performed Welch's *t*-test for the three samples of Lidar and the ATL08-Terrain product (i.e. strong beams, weak beams, and all beams). The results of the test are shown in Figure 10 and Table 10.

Table 10 shows that the ATL08-Terrain product and the Lidar DTM nearly have the same mean elevation and the same STD for the different ATL08 beams'

Table 8. Accuracy assessment of ASTER, SRTM, and TDX DEMs by 10,000 LiDAR DTM points.

DEM	ASTER	SRTM	TDX
RMSE (m)	11.683	12.834	10.494
MAE (m)	9.119	11.340	8.318
STD (m)	145.834	144.136	143.536
Mean (m)	2501.363	2505.956	2501.463
Median (m)	2530.155	2533.225	2528.404

Table 9. Accuracy assessment of ASTER, SRTM, and TDX DEMs by the ATL08 strong and weak beams and corresponding LiDAR DTM points. (Δ = DEM (Lidar RMSE) − DEM (ATL08 RMSE)).

DEM \ RMSE (m)	Lidar_s	ATL08_s	Δs	Lidar_w	ATL08_w	Δw	Lidar_All	ATL08_All	Δ All
ASTER	11.28	11.113	0.167	9.306	9.044	0.262	10.924	10.742	0.182
SRTM	12.824	12.626	0.198	11.453	11.114	0.339	12.569	12.346	0.223
TDX	10.311	10.141	0.17	7.408	7.101	0.307	9.813	9.625	0.188

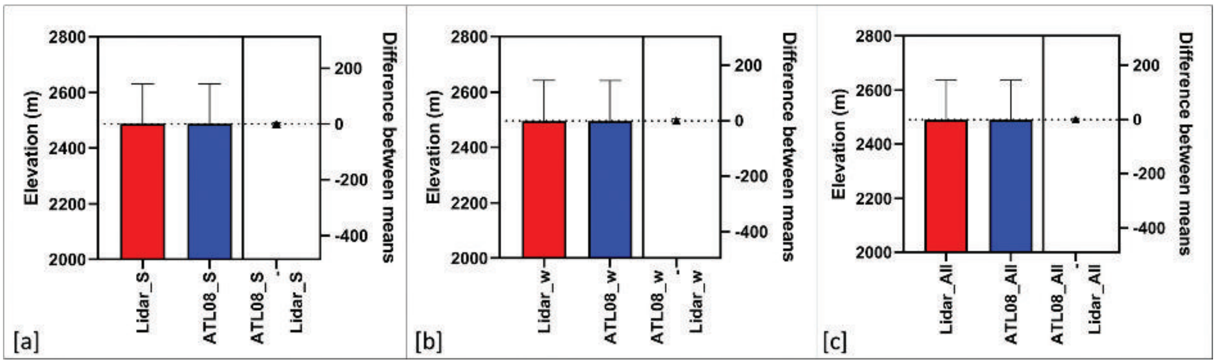

Figure 10. Bar graphs showing the mean elevations of the lidar DTM and the ATL08-terrain product as well as the independent *t*-test results (difference between means) for the samples. a) strong beams, b) weak beams, c) all beams.

Table 10. T-test results for the ATL08-terrain elevations of the strong beams, weak beams and all beams, and the corresponding Lidar DTM elevations.

Beams	Group/N	Mean	STD	*t*	*p*
Strong	Lidar/3463	2487.1768	144.4271	−0.004	0.997
	ATL08/3463	2487.1899	144.5855		
Weak	Lidar/2957	2497.2783	144.8459	0.149	0.881
	ATL08/2957	2496.7152	144.1259		
All	Lidar/6420	2491.8295	144.6964	0.099	0.921
	ATL08/6420	2491.5772	144.9012		

energy. At 95% confidence level, the *p* values for the strong beams, weak beams, and all beams are greater than 0.05 which means there is no significance and null hypotheses cannot be rejected. This shows that there is no difference between the means of the ATL08 and Lidar samples which also can be clearly distinguished in Figure 9(a–c). The results in Table 10 and Figure 10 strengthen our theory about the possibility of using the ATL08 product as reference data while performing almost the same as the Lidar DTM when the Lidar data is not available over a specific area.

Although the results of our study show that the ATL08 terrain product can be used as a vertical reference, some issues may prohibit its use in other areas. For instance, the ATL08 terrain heights may contain the reflectance of some trees or artificial features (i.e. buildings) or noise which reduces the vertical accuracy of the ATL08 product. These errors are magnified in the ATL08 canopy product and gradually decrease in the terrain product as terrain photons have a higher density and more continuous pattern than the canopy. The work with the ATLAS weak beam can contain more height sampling errors. In addition, the areas covered by this beam mostly contain (no-data); hence, researchers often reject the use of this data in their studies (Liu, Cheng, and Chen 2021; Neuenschwander et al. 2020). Consequently, this reduces the actual spatial coverage of the ATL08 product over the study area in question. Theoretically, the ATL08 should provide elevation values every 100 m. However, due to the fewer number of reflectance photons from the ground surface over particular areas, the ATL08 terrain product may have some gaps thus leading to complications when detecting the detailed shape of the Earth's surface. Moreover, interpolation methods will not increase the accuracy of the elevations, since they cannot add more detail, especially in areas with rough terrain (Liu, Popescu, and Malambo 2020).

When examining which set of beams is most useful for global DEM assessment, both strong and weak beams provided very good results separately and together, and equivalent to results generated from 10,000 DTM LiDAR points distributed over a broad area. The strong beams however, had the highest accuracy (RMSE <0.6 m) for all DEMs, and the weak beams accuracy was the lowest (RMSE from 1.7 m to 3.4 m) for all DEMs, while the accuracy of all beams together for all DEMs was higher than the weak beams alone (RMSE from 0.5 m to 0.9 m). These results agree with previous studies that found that the accuracy of the strong beams was better than the weak beams (Yu et al. 2021). Therefore, we recommend the use of only strong beams in a DEM evaluation process over a target study area when there are a large number of strong beams available. Otherwise, both strong and weak beams can be used together. We do not recommend the of use of only weak beams for DEM evaluation.

6. Conclusions

In this study, we examined the ATL08 accuracy to validate the elevations of the ASTER V3, SRTM V3 and TDX V1 DEMs. In addition, we studied terrestrial factors affecting the ATL08 height errors and height uncertainty (i.e. slope, aspect, and land cover). Regardless of the low spatial coverage of the ATL08 observations (100 m spatial resolution, 14 m beam footprint, and 3 km separation between pair tracks) (Zhang et al. 2021), the ATL08 showed strong potential as a height reference for the 30 m resolution ASTER, 30 m resolution SRTM and 90 m resolution TDX DEMs over a vegetated mountain area with complex topography. The terrain height uncertainty can be used to filter the ATL08 terrain observations; and consequently, enhance the accuracy of the ATL08 by eliminating the high values of uncertainty (in our study >20 m) while keeping the reliable elevation measurements. We found that slope and vegetation cover can increase the height uncertainty (>800 m and >200 m) and the height errors (>16 m and >12 m) for weak and the strong beams, respectively; but terrain aspect did not have a significant effect on both ATL08 strong and weak beams after filtering their height observations. A very low threshold of uncertainty (<20 m) to filter the elevations in the vegetated mountainous area can significantly decrease the number of the ATL08 terrain observations, especially, for the weak beams. To summarize, the ATL08 strong beams can provide an accuracy at the sub-meter level and close to that achieved from a large number of DTM LiDAR points distributed over a study area. Therefore, we recommend strong beams as a height reference over the mountainous regions with dense vegetation cover, but adding weak beam observations to the strong beams can degrade the ATL08 accuracy.

Disclosure statement

No potential conflict of interest was reported by the author(s).

Funding

This work was supported in part by the National Natural Science Foundation of China under grant of 42090012, in part by the project supported by the Open Fund of Hubei Luojia Laboratory (220100009), in part by 03 special research and 5G project of Jiangxi province in China (20212ABC03A09); Zhuhai industry university research cooperation project of China (ZH22017001210098PWC); Sichuan Science and Technology Program (2022YFN0031), and Zhizhuo Research Fund on Spatial-Temporal Artificial Intelligence (Grant No. ZZJJ202202).

Notes on contributors

Nahed Osama received her MSC degree from Wuhan University. She is currently a PhD scholar at LIESMARS, Wuhan University. Her research interests are photogrammetry and remote sensing, information extraction, land observations and analysis.

Zhenfeng Shao received his PhD degree from Wuhan University. He is a full professor at LIESMARS, Wuhan University. His research interests include urban remote sensing, impervious surfaces, information extraction, environmental monitoring, big data, image classification, deep learning.

Yue Ma is an associate professor at school of electronic information, Wuhan University. His research interests are Optics, Oceanography, and Remote Sensing.

Jianguo Yan received his PhD degree from Wuhan University. He is a professor at LIESMARS, Wuhan University. His research interests include Satellite geodesy, Planetary spacecraft precise orbit determination, Planet gravity field recovery, and Planet interior structure research.

Yewen Fan is an associate professor at LIEMSARS, Wuhan University. His research interests are GIS applications.

Shaimaa Magdy Habib received her MSC degree from Cairo university, Egypt. She is a research assistant at the National Authority for Remote Sensing and Space sciences (NARSS), Egypt. Her research interests are remote sensing and GIS, and their applications in renewable energy.

Mohamed Freeshah received a PhD degree from Wuhan University. He is currently a post-doctor fellow at SGG, Wuhan University. His research interests include Interdisciplinary studies in Earth system science.

ORCID

Nahed Osama http://orcid.org/0000-0002-1812-0890
Zhenfeng Shao http://orcid.org/0000-0003-4587-6826
Yue Ma http://orcid.org/0000-0003-1241-8650
Jianguo Yan http://orcid.org/0000-0003-2612-4776
Shaimaa Magdy Habib http://orcid.org/0000-0002-2457-7344
Mohamed Freeshah http://orcid.org/0000-0003-3539-7450

Data availability statement

All the data used in this study are for free and publicly available. The ATL08 data, ASTER DEM, and SRTM DEM were provided by The National Aeronautics and Space Administration through this link https://doi.org/10.1080/10095020.2022.2087108. While, the TDX DEM was provided by the German Aerospace Center (DLR) through this link https://doi.org/10.1080/10095020.2022.2087108. The validation data is available through The OpenTopography website through this link https://doi.org/10.1080/10095020.2022.2087108.

References

Abrams, M., R. Crippen, and H. Fujisada. 2020. “ASTER Global Digital Elevation Model (GDEM) and ASTER Global Water Body Dataset (ASTWBD).” *Remote Sensing* 12 (7): 1–12. doi:10.3390/rs12071156.

Arefi, H., and P. Reinartz. 2011. "Accuracy Enhancement of ASTER Global Digital Elevation Models Using ICESat Data." *Remote Sensing* 3 (7): 1323–1343. doi:10.3390/rs3071323.

Asal, F. 2019. "Creation and Analysis of Earth's Surface Roughness Maps from Airborne LiDar Measurements in Downtown Urban Landscape." *Journal of Geographic Information System* 11 (02): 212–238. doi:10.4236/jgis.2019.112015.

Athmania, D., and H. Achour. 2014. "External Validation of the ASTER GDEM2, GMTED2010 and CGIAR-CSI-SRTM V4.1 Free Access Digital Elevation Models (DEMs) in Tunisia and Algeria." *Remote Sensing* 6 (5): 4600–4620. doi:10.3390/rs6054600.

Bangen, S.G. 2013. "Comparison of Topographic Surveying Techniques in Streams." MSc Diss., UTAH STATE UNIVERSITY Logan, Utah.

Boulton, S. J., and M. Stokes. 2018. "Which DEM is Best for Analyzing Fl Uvial Landscape Development in Mountainous Terrains ?" *Geomorphology* 310: 168–187. doi:10.1016/j.geomorph.2018.03.002.

Braun, A., and G. Fotopoulos. 2007. "Assessment of SRTM, ICESat, and Survey Control Monument Elevations in Canada." *Photogrammetric Engineering and Remote Sensing* 73 (12): 1333–1342. doi:10.14358/PERS.73.12.1333.

Brenner, A.C., J.P. DiMarzio, and H.J. Zwally. 2007. "Precision and Accuracy of Satellite Radar and Laser Altimeter Data Over the Continental Ice Sheets." *IEEE Transactions on Geoscience and Remote Sensing* 45 (2): 321–331. doi:10.1109/TGRS.2006.887172.

Brunt, K., T. Neumann, and C. Larsen. 2019. "Assessment of Altimetry Using Ground-Based GPS Data from the 88S Traverse, Antarctica, in Support of Icesat-2." *The Cryosphere* 13: 579–590. doi:10.5194/tc-13-579-2019.

Carabajal, C.C., and J.P. Boy. 2020. "ICESat-2 Altimetry as Geodetic Control." *International Archives of the Photogrammetry, Remote Sensing and Spatial Information Sciences - ISPRS Archives* 43 (B3): 1299–1306. doi:10.5194/isprs-archives-XLIII-B3-2020-1299-2020.

Dandabathula, G., and M. Verma. 2020. "Evaluation of Best-Fit Terrain Elevation of Icesat-2 ATL08 Using DGPS Surveyed Points." *Journal of Applied Geodesy* 14 (3): 2–3. doi:10.1515/jag-2020-0003.

Dong, Y., L. Zhang, H. Jiang, T. Balz, and M. Liao. 2021. "Cascaded Multi-Baseline Interferometry with Bistatic TerraSar-X/tandem-X Observations for DEM Generation." *ISPRS Journal of Photogrammetry and Remote Sensing* 171: 224–237. doi:10.1016/j.isprsjprs.2020.11.012.

Farr, T.G., and M. Kobrick. 2000. "Shuttle Radar Topography Mission Produces a Wealth of Data." *Eos* 81 (48): 583–585. doi:10.1029/EO081i048p00583.

Fricker, H.A., A. Borsa, B. Minster, C. Carabajal, K. Quinn, and B. Bills. 2005. "Assessment of ICESat Performance at the Salar de Uyuni, Bolivia." *Geophysical Research Letters* 32 (21): 1–5. doi:10.1029/2005GL023423.

Guth, P. L. 2010. "Geomorphometric Comparison of Aster Gdem and Srtm." In *Geospatial Data and Geovisualization: Environment, Security, and Society*, edited by M. Madden and E. Lynn Usery. Vol. 10. Orlando, FL: A special joint symposium of 1110 ISPRS Technical Commission IV & AutoCarto - ASPRS/ CaGIS 2010 Fall Specialty Confe rence, November 15-19. https://www.isprs.org/proceedings/XXXVIII/part4/files/Guth.pdf

Guth, P.L., and T.M. Geoffroy. 2021. "LiDar Point Cloud and ICESat-2 Evaluation of 1 Second Global Digital Elevation Models: Copernicus Wins." *Transactions in GIS* 25 (5): 2245–2261. doi:10.1111/tgis.12825.

Henrys, P.A., and S.G. Jarvis. 2019. "Integration of Ground Survey and Remote Sensing Derived Data: Producing Robust Indicators of Habitat Extent and Condition." *Ecology and Evolution* 9 (14): 8104–8112. doi:10.1002/ece3.5376.

Hsu, H., C. Huang, M. Jasinski, Y. Li, H. Gao, T. Yamanokuchi, C. Wang, et al. 2021. "A Semi-Empirical Scheme for Bathymetric Mapping in Shallow Water by ICESat-2 and Sentinel-2 : A Case Study in the South China Sea". *ISPRS Journal of Photogrammetry and Remote Sensing* 178: 1–19. 10.1016/j.isprsjprs.2021.05.012.

Hueso González, J., M. Bachmann, R. Scheiber, and G. Krieger. 2010. "Definition of Icesat Selection Criteria for Their Use as Height References for Tandem-X." *IEEE Transactions on Geoscience and Remote Sensing* 48 (6): 2750–2757. doi:10.1109/TGRS.2010.2041355.

Lin, X., M. Xu, C. Cao, Y. Dang, B. Bashir, B. Xie, and Z. Huang. 2020. "Estimates of Forest Canopy Height Using a Combination of ICESat-2/ATLAS Data and Stereo-Photogrammetry." *Remote Sensing* 12 (3649): 21. doi:10.3390/rs12213649.

Liu, A., X. Cheng, and Z. Chen. 2021. "Performance Evaluation of GEDI and ICESat-2 Laser Altimeter Data for Terrain and Canopy Height Retrievals." *Remote Sensing of Environment* 264: 112571. doi:10.1016/j.rse.2021.112571.

Liu, M., S. Popescu, and L. Malambo. 2020. "Feasibility of Burned Area Mapping Based on ICESAT-2 Photon Counting Data." *Remote Sensing* 12 (24): 18. doi:10.3390/RS12010024.

Liu, Z., J. Zhu, H. Fu, C. Zhou, and T. Zuo. 2020. "Evaluation of the Vertical Accuracy of Open Global Dems Over Steep Terrain Regions Using Icesat Data: A Case Study Over Hunan Province, China." *Sensors* 20 (17): 1–16. doi:10.3390/s20174865.

Magruder, L., A. Neuenschwander, and B. Klotz. 2021. "Digital Terrain Model Elevation Corrections Using Space-Based Imagery and ICESat-2 Laser Altimetry." *Remote Sensing of Environment* 264: 112621. doi:10.1016/j.rse.2021.112621.

Magruder, L. A., and K. M. Brunt. 2018. "Performance Analysis of Airborne Photon-Counting Lidar Data in Preparation for the ICESat-2 Mission." *IEEE Transactions on Geoscience and Remote Sensing* 56 (5): 2911–2918. doi:10.1109/TGRS.2017.2786659.

NASA. 2015. "The Shuttle Radar Topography Mission (SRTM) Collection User Guide." https://lpdaac.usgs.gov/sites/default/files/public/measures/docs/NASA_SRTM_V3.pdf.

Neuenschwander, A., E. Guenther, J.C. White, L. Duncanson, and P. Montesano. 2020. "Validation of ICESat-2 Terrain and Canopy Heights in Boreal Forests." *Remote Sensing of Environment* 251: 112110. doi:10.1016/j.rse.2020.112110.

Neuenschwander, A.L., and L.A. Magruder. 2016. "The Potential Impact of Vertical Sampling Uncertainty on ICESat-2/ATLAS Terrain and Canopy Height Retrievals for Multiple Ecosystems." *Remote Sensing* 8 (12): 1039. doi:10.3390/rs8121039.

Neuenschwander, A., and K. Pitts. 2019. "The ATL08 Land and Vegetation Product for the ICESat-2 Mission." *Remote Sensing of Environment* 221: 247–259. doi:10.1016/j.rse.2018.11.005.

Neuenschwander, A., K. Pitts, B. Jelley, J. Robbins, B. Klotz, S. Popescu, R. Nelson, D. Harding, D. Perderson, and R. Sheridan. 2019. *ICESat-2 Algorithm Theoretical Basis Document for Land-Vegetation Along-Track Products (ATL08) Release 002*. Vol. 2. Boulder, CO: NASA National

Snow and Ice Data Center Distributed Active Archive Center. https://icesat-2.gsfc.nasa.gov/sites/default/files/page_files/ICESat2_ATL08_ATBD_r002_v2.pdf

Neumann, T.A., A.J. Martino, T. Markus, S. Bae, M.R. Bock, A.C. Brenner, K.M. Brunt, et al. 2019. "The Ice, Cloud, and Land Elevation Satellite – 2 Mission: A Global Geolocated Photon Product Derived from the Advanced Topographic Laser Altimeter System". *Remote Sensing of Environment* 233: 111325. 10.1016/j.rse.2019.111325.

Osama, N., B. Yang, Y. Ma, and M. Freeshah. 2021. "A Digital Terrain Modeling Method in Urban Areas by the ICESat-2 (Generating Precise Terrain Surface Profiles from Photon-Counting Technology)." *Photogrammetric Engineering & Remote Sensing* 87 (4): 237–248. doi:10.14358/pers.87.4.237.

Popescu, S.C., T. Zhou, R. Nelson, A. Neuenschwander, R. Sheridan, L. Narine, and K.M. Walsh. 2018. "Photon Counting LiDar: An Adaptive Ground and Canopy Height Retrieval Algorithm for ICESat-2 Data." *Remote Sensing of Environment* 208: 154–170. doi:10.1016/j.rse.2018.02.019.

Ravibabu, M.V., K. Jain, S.P. Singh, and N.J. Meeniga. 2010. "Accuracy Improvement of ASTER Stereo Satellite Generated DEM Using Texture Filter." *Geo-Spatial Information Science* 13 (4): 257–262. doi:10.1007/s11806-010-0376-9.

Saini, O., A. Bhardwaj, and R. S. Chatterjee. 2019. "Generation of Radargrammetric Digital Elevation Model (DEM) and Vertical Accuracy Assessment Using Icesat-2 Laser Altimetric Data and Available Open-Source Dems." In *39th INCA International Congress on New Age Cartography and Geospatial Technology in Digital India*, December 18–20, edited by Sh. N. Tomar, 166.Dehradun, India. http://www.incaindia.org/images/uploads/documents/Indian%20Cartographer%20Vol.39%202019.pdf

Salas, E.A.L. 2021. "Waveform LiDar Concepts and Applications for Potential Vegetation Phenology Monitoring and Modeling: A Comprehensive Review." *Geo-Spatial Information Science* 24 (2): 179–200. doi:10.1080/10095020.2020.1761763.

Satgé, F., M.P. Bonnet, F. Timouk, S. Calmant, R. Pillco, J. Molina, W. Lavado-Casimiro, A. Arsen, J.F. Crétaux, and J. Garnier. 2015. "Accuracy Assessment of SRTM V4 and ASTER GDEM V2 Over the Altiplano Watershed Using ICESat/glas Data." *International Journal of Remote Sensing* 36 (2): 465–488. doi:10.1080/01431161.2014.999166.

Siegfried, M.R., R.L. Hawley, and J.F. Burkhart. 2011. "High-Resolution Ground-Based GPS Measurements Show Intercampaign Bias in ICESat Elevation Data Near Summit, Greenland." *IEEE Transactions on Geoscience and Remote Sensing* 49 (9): 3393–3400. doi:10.1109/TGRS.2011.2127483.

Slater, J.A., G. Garvey, C. Johnston, J. Haase, B. Heady, G. Kroenung, and J. Little. 2006. "The SRTM Data 'Finishing' Process and Products." *Photogrammetric Engineering and Remote Sensing* 72 (3): 237–247. doi:10.14358/PERS.72.3.237.

Tian, X., and J. Shan. 2021. "Comprehensive Evaluation of the ICESat-2 ATL08 Terrain Product." *IEEE Transactions on Geoscience and Remote Sensing* 59 (10): 8195–8209. doi:10.1109/TGRS.2021.3051086.

Vernimmen, R., A. Hooijer, and M. Pronk. 2020. "New Icesat-2 Satellite Lidar Data Allow First Global Lowland Dtm Suitable for Accurate Coastal Flood Risk Assessment." *Remote Sensing* 12 (17): 1–17. doi:10.3390/rs12172827.

Wang, C., X. Zhu, S. Nie, X. Xi, D. Li, W. Zheng, and S. Chen. 2019. "Ground Elevation Accuracy Verification of ICESat-2 Data: A Case Study in Alaska, USA." *Optics Express* 27 (26): 38168. doi:10.1364/oe.27.038168.

Wu, J., Q. Yang, and Y. Li. 2018. "Partitioning of Terrain Features Based on Roughness." *Remote Sensing* 10 (12): 1–21. doi:10.3390/rs10121985.

Yu, J., S. Nie, W. Liu, X. Zhu, D. Lu, W. Wu, and Y. Sun. 2021. "Accuracy Assessment of ICESat-2 Ground Elevation and Canopy Height Estimates in Mangroves." *IEEE Geoscience and Remote Sensing Letters* 19: 1–5. doi:10.1109/LGRS.2021.3107440.

Zhang, J., Q. Hu, Y. Li, H. Li, and J. Li. 2021. "Area, Lake-Level and Volume Variations of Typical Lakes on the Tibetan Plateau and Their Response to Climate Change, 1972–2019." *Geo-Spatial Information Science* 24 (3): 458–473. doi:10.1080/10095020.2021.1940318.

Zhang, K., D. Gann, M. Ross, Q. Robertson, J. Sarmiento, S. Santana, J. Rhome, and C. Fritz. 2019. "Accuracy Assessment of ASTER, SRTM, ALOS, and TDX Dems for Hispaniola and Implications for Mapping Vulnerability to Coastal Flooding." *Remote Sensing of Environment* 225 (February): 290–306. doi:10.1016/j.rse.2019.02.028.

Zhang, W., N. Xu, Y. Ma, B. Yang, Z. Zhang, X. H. Wang, and S. Li. 2021. "A Maximum Bathymetric Depth Model to Simulate Satellite Photon-Counting Lidar Performance." *ISPRS Journal of Photogrammetry and Remote Sensing* 174: 182–197. doi:10.1016/j.isprsjprs.2021.02.013.

Zhu, X., S. Nie, C. Wang, X. Xi, D. Li, G. Li, P. Wang, D. Cao, and X. Yang. 2020. "Estimating Terrain Slope from ICESat-2 Data in Forest Environments." *Remote Sensing* 12 (20): 1–19. doi:10.3390/rs12203300.